Received: 6 February 2020 | Revised: 19 August 2020 | Accepted: 20 October 2020

DOI: 10.1002/joc.6905

RESEARCH ARTICLE

International Journal of Climatology RMetS

Increasing energy transfer over Eurasia and the North Atlantic enhancing the Eurasian low-frequency wave and boreal summer droughts in China

Jie Zhang[1] | **Siwen Zhao**[2] | **Zhiheng Chen**[1]

[1]Key Laboratory of Meteorological Disaster, Ministry of Education (KLME)/ Joint International Research Laboratory of Climate and Environment Change (ILCEC)/Collaborative Innovation Center on Forecast and Evaluation of Meteorological Disasters (CIC-FEMD), Nanjing University of Information Science & Technology, Nanjing, China

[2]Institute of Atmospheric Environment, China Meteorological Administration, Shenyang, China

Correspondence
Jie Zhang, Key Laboratory of Meteorological Disaster, Ministry of Education (KLME)/Joint International Research Laboratory of Climate and Environment Change (ILCEC)/ Collaborative Innovation Center on Forecast and Evaluation of Meteorological Disasters (CIC-FEMD), Nanjing University of Information Science & Technology, Nanjing 210044, China.
Email: gs-zhangjie@163.com

Funding information
Priority Academic Program Development of the Jiangsu Higher Education Institutions; National Natural Science Foundation of China for Key Program, Grant/Award Number: 41975083; National Key R&D Program of China, Grant/Award Number: 2018YFC1507101

Abstract

The prolonged droughts that frequently occur in northern China are related to persistent anomalies of circulation and the low-frequency waves. To explore the formation of the low-frequency waves and the related internal variability and external forcing, the intra-seasonal kinetic energy (KE) and the corresponding energy transfer terms are investigated algorithmically with multiscale energy and vorticity analysis. The results show two major energy sources located over the central North Atlantic (NA) and Europe, with increasing baroclinicity and energy conversion. The major energy conversion is from basic flow to intra-seasonal KE, which corresponds to a southeastern extension of NA jet stream (JS) exit and the northward shift in the entrance of Afro Asian JS. JS shifts are helpful to the conjunction of both JS, and thereby enhance JS waveguide and wave energy dispersion. In addition, with increasing surface temperature and diabatic heating over Europe and the Mediterranean Sea, there are increase baroclinicity that facilitates the buoyancy energy conversion, ascending KE flux and positive pressure flux in the lower troposphere, those result in higher mid-upper-troposphere KE. The divergent energy contributes to the development and enhancement of the low-frequency waves, favouring the extratropical eddy, wave structure, and quasi-stationary waves amplitude, which is thereby conducive to magnified wave amplitude and extreme droughts in northern China. The results emphasize the internal dynamics and local forcing and provide prediction reference for extratropical extremes.

KEYWORDS

extreme drought, kinetic energy, low-frequency wave, multiscale energy transfer

1 | INTRODUCTION

Rainfall in northern China (NC) is mainly concentrated on the high summer (July and August, JA), contributive to more than 50% of annual rainfall (Zhang *et al*., 2019a). However, prolonged droughts with more than 15 consecutive dry days (CDDs, Frich *et al*., 2002) have frequently occurred in NC over past two decades (Zhang *et al*., 2015; Zhang *et al*., 2019a), which could directly influence water storage and utilization in NC and threaten people's

production and life. However, the prediction of such extratropical climate and extremes are poor. To understand the causes of such successive droughts is helpful to disaster prevention and mitigation. Previous studies have shown that droughts in NC are related to persistent anomalies of multiscale circulation, such as the weakened East Asian summer monsoon (EASM) linked to low-frequency variations in the tropical forcing sources (Coumou and Rahmstorf, 2012; Kosaka and Xie, 2013; Kamae *et al*., 2014; Trenberth *et al*., 2014; Wang *et al*., 2014). The main forces include the Pacific Decadal Oscillation, the tropical sea surface temperature (SST) of the Indo-Pacific, the Tibetan Plateau thermal forcing and sea-land thermodynamic contrast (Qian and Zhou, 2013; Zhang *et al*., 2019b), all of which determine water vapour transport and convergence positions (Ueda *et al*., 2015). However, large uncertainties remain concerning the effects of the summer monsoon and SST on the droughts/flooding in NC (Zhang *et al*., 2018a; Zhang *et al*., 2018b; Zhang *et al*., 2019b).

Previous studies have shown that the amplifications of quasi-stationary waves dominate the extratropical extreme of weather and climate in the Northern Hemisphere (Hoskins and Ambrizzi, 1993; Ambrizzi *et al*., 1995; Hoskins and Woollings, 2015; Zhuo *et al*., 2016; Zhang *et al*., 2019a), such as the blocking high, being conducive to the occurrence of extreme weather (Ju *et al*., 2005; Hu and Feng, 2008; Zhao *et al*., 2010; Huang *et al*., 2015). As for climate extreme, one of the main causes is the anomalous position of the westerly JS with meridional temperature gradient, Arctic ice degradation, and climate warming (Petoukhov *et al*., 2013; Wang *et al*., 2014). The climate extremes are also possibly associated with the multiscale North Atlantic SST (Sutton and Hodson, 2005). However, how North Atlantic SST and other forcing influences quasi-stationary wave anomalies are still lack of physical explanation.

The quasi-stationary wave anomalies are influenced by the low-frequency waves and transient eddy imposed on free quasi-stationary waves (Petoukhov *et al*., 2016). Thus the enhancing low-frequency wave is identified an important cause of anomalous extratropical temperature and rainfall in summer (Ambrizzi *et al*., 1995; Lau and Weng, 2002; Hoskins and Woollings, 2015), and the extremes include the American droughts/floods in 1988 and 1993, the European heatwave in 2003, the Russia heatwaves in 2010 and 2014 (Schubert *et al*., 2014; Wang and He, 2015). Zhang *et al*. (2019a) noted that the low-frequency wave in the mid-high latitude exhibited a decadal abrupt after 1990s, which enhanced Eurasian teleconnection (EU) pattern over the mid-high latitudes due to increasing resonant probability; therefore, it is worthy of considering the variation mechanism of the low-frequency wave, so as to exploring the cause of extremes. Previous results have shown that the mid-latitude waves respond to the tropical SST, linking to deep convective activity over the western North Pacific and the Indian Ocean (Sato and Takahashi, 2006; Ding and Wang, 2007); however, the tropical SST and convection cannot entirely interpret the multi-scale changes of EU pattern in recent years, implying the effect of other forcing and internal dynamics on the low-frequency waves (Zhang *et al*., 2019a).

From the perspective of dynamics, the low-frequency wave variation is related to the low-frequent wave and transient eddy and transient wave flux (Schubert *et al*., 2010). As land sea distribution leading to the location of the North Atlantic JS exit and the entrance of Afro Asian JS, the NA, and Western Europe region is a part of the energy sources (Ding and Wang, 2007). The dynamic effect of the JS waveguide enhances the low-frequency wave (Hoskins and Woollings, 2015), and the waveguide ability is sensitive to the JS position, width and speed (Manola *et al*., 2013). With global warming, Arctic ice loss reduces the temperature gradient that leads to northward shift of the JS (Schneider *et al*., 2015), thereby changes the energy transfer and low-frequency waves. However, little is known about how low-frequency waves changed.

From the perspective of thermodynamics, the occurrences, developments and maintenances of low-frequency waves are influenced by non-uniform heating and thermal forcing. A positive North Atlantic Oscillation (NAO), associated with the North Atlantic SST mode, excites a high-latitude Rossby wave train, which modulates the Ural high, Okhotsk blocking high (Wu *et al*., 2012) and a mid-latitude Eurasian wave train via the Tibetan Plateau (Sato and Takahashi, 2006; Xin *et al*., 2010; Cui *et al*., 2015). Previous studies also suggested that the Atlantic Multidecadal Oscillation (AMO) could excite the Silk Road Pattern-like responses and impact on the Eurasian nonuniform warming could increase the baroclinicity and energy conversion (Sun *et al*., 2019; Zhang *et al*., 2020).

The land memorizes the effect of SST forcing in winter and spring, which further impacts the low-frequency wave in summertime, acting as a land "bridge" (Wang and Kumar, 1998; Guo *et al*., 2011). The high snow cover over Tibetan Plateau in spring leads to decreasing sensible heat flux in summer, which changes the mid-latitude wave phase (Zhang *et al*., 2018a; Zhang *et al*., 2018b). With climate warming, the non-uniform heating of the

Eurasian surface enhances the atmospheric baroclinicity in the troposphere (Zhang *et al*., 2019a), which could influence the low-frequency wave and rainfall related EASM (Chen *et al*., 2017). The thermal anomalies and deep convection over Eurasia (Western Europe and Western Asia) are responsible for enhancement of Eurasian low-frequency wave (Sato and Takahashi, 2006; Zhang *et al*., 2019a), which is triggered into the JS waveguide on the northern side of the Tibetan Plateau (Hoskins and Woollings, 2015).

In summary, the low-frequency wave linked to the extremes over Eurasia responds to internal dynamics and thermodynamics anomalies. Consequently, given that enhanced extremes occurred after 1990s, the causes of the decadal low-frequency waves should be investigated thoroughly. Considering that successive droughts correspond to prolonging CDD beyond biweekly duration (Zhang *et al*., 2015, 2019a), this study aims to investigate low-frequency waves and circulation anomalies at the intra-seasonal scale, as well as the kinetic energy (KE) and the possible forcing. The paper determines all of the energy transfer terms quantitatively to delineate the energy transport and transfer, to reveal the thermodynamic and dynamic processes, and the effect on the low-frequency wave.

2 | DATA AND METHODS

2.1 | Datasets

The reanalysis dataset is the interim daily data from the European Center Medium-Range Weather Forecasts (ECMWF) (http://apps.ecmwf.int/datasets/) with a horizontal resolution of $0.75^\circ \times 0.75^\circ$ (Dee *et al*., 2011). The data of geopotential height and velocity are applied. Considering the water resource stress is of great concern in NC (defined as 105–120°E, 35–45°N), circulation and energy transfer related to JA drought are analysed.

2.2 | Models and other methods

The linear baroclinic model (LBM) is employed to simulate atmospheric responses to an idealized forcing of diabatic heating over Europe. The LBM has a triangular truncation of 21 waves and a vertical resolution of 20 levels (Watanabe and Kimoto, 2000). The background state in the experiment is the JA climatology of 1979–2015 from the ECMWF/interim reanalysis. Given that significant increasing baroclinicity over central and western Europe, and there are large positive KE and divergent energy, the forcing centre is situated over Europe (47°N and 20°E) at 700 hPa with a horizontal scale of 12°E × 6°N and is set to 6 K/day. The integration time of the model is set to 30 days, because simulated circulations response to forcing could approach the steady state after the 15th days, and the data during the 15-30th days could be used for analysing circulation characters.

The localized multiscale energy and vorticity analysis (MS-EVA, Liang and Robinson, 2005) from which a theory of localized finite-amplitude baroclinic and barotropic instabilities has been developed to calculate the multiscale energetics. MS-EVA is based on a new functional analysis tool known as the multiscale window transform (MWT; Liang and Anderson, 2007), which can be used to decompose a function space into several orthogonal subspaces, each of which exclusively spans a range of time scale, while the local temporal characteristics of the resulting energetics are retained. Recently, MS-EVA has been systematically extended to and reformulated in a generic setting for both atmospheres and oceans (Liang, 2016); particularly, the rigorously established theory of canonical transfer allows for a natural and unique separation of the intra-scale and cross-scale energy transfers from the intertwined nonlinear processes. With MWT, the KE and available potential energy (APE) densities for the windows of intra-seasonal scale (ϖ) can be defined. The multiscale equation for the KE at ϖ scale is shown as follows:

$$\begin{aligned}\frac{\partial \mathrm{K}^{\varpi}}{\partial \mathrm{t}} = &\underbrace{-\nabla\cdot\left[\frac{1}{2}\widehat{(vv_h)}^{\sim\varpi}\cdot\widehat{\mathrm{v}}_h^{\sim\varpi}\right]}_{\nabla\cdot\mathrm{Q}_K^{\varpi}} + \underbrace{\frac{1}{2}\left[\widehat{(vv_h)}^{\sim\varpi}:\widehat{\mathrm{v}}_h^{\sim\varpi} - \nabla\cdot(vv_h)^{\sim\varpi}\cdot\widehat{\mathrm{v}}_h^{\sim\varpi}\right]}_{\Gamma_K^{\varpi}} \\ &\underbrace{-\nabla\cdot\left[\widehat{\mathrm{v}}^{\sim\varpi}\widehat{\Phi}^{\sim\varpi}\right]}_{\nabla\cdot\mathrm{Q}_P^{\varpi}} - \underbrace{\left[\widehat{\omega}^{\sim\varpi}\widehat{\alpha}^{\sim\varpi}\right]}_{\mathrm{b}^{\varpi}} + D \\ &= Q_K + \left(\mathrm{K}_{\mathrm{s}-\varpi}^{\varpi} + \mathrm{K}_{\mathrm{m}-\varpi}^{\varpi}\right) + Q_P + B + D\end{aligned} \tag{1}$$

where, K^{ϖ} is KE on the intra-seasonal scale ϖ;∇ is divergences; Q_K^{ϖ} is flux of KE on the scale ϖ; Γ_K^{ϖ} is canonical transfer of KE from synoptic scale ($K_{s-\varpi}^{\varpi}$, eddy) and climatic scale ($K_{m-\varpi}^{\varpi}$, basic flow) to the scale ϖ; Q_P^{ϖ} is pressure working rate; b^{ϖ} is the rate of buoyangcy conversion, it is defined to be positive if it is from KE to APE; D is friction dissipation; For details of the other parameters, refer to Liang et al.(2016). In order to exhibit these terms and understand the contribution to increasing $\partial K/\partial t$, $-\nabla\cdot Q_K^{\varpi}$ is redefined as Q_K, standing for vertical kinetic transfer due to divergence/convergence; $-\nabla\cdot Q_P^{\varpi}$ is redefined as Q_P, standing for positive kinetic transfer due to pressure work; $-b^{\varpi}$ is redefined as B, it is positive if it is converted from APE to KE. All of the KE and the related terms are calculated by using MS-EVA. Concerning that 2^n days set in the MS-EVA, the intra-seasonal scale in the study is defined as the period between 8 (2^3) and 64 (2^6) days, the period of synoptic scale is less than 8 (2^3) days. To further delineate the energy transport and transfer processes, we quantitatively determine all of the energy transfer terms.

The wave activity flux (WAF) is useful for diagnostic and illustrating stationary or migratory quasi-geostrophic wave disturbances and for revealing where anomalous waves are emitted, absorbed and transferred (Takaya and Nakamura, 2001). It is showed as:

$$\mathrm{WAF}=\frac{\mathrm{p}}{2|\mathrm{U}|}\begin{pmatrix}\mathrm{U}\left(\psi'_x-\psi'\psi'_{xx}\right)+\mathrm{V}\left(\psi'_x\psi'_y-\psi'\psi'_{xy}\right)\\ \mathrm{U}\left(\psi'_x\psi'_y-\psi'\psi'_{xy}\right)+\mathrm{V}\left(\psi'^{\mathrm{V}}_y-\psi'\psi'_{yy}\right)\\ \frac{f_0^2}{N^2}\left[\mathrm{U}\left(\psi'_x\psi'_z-\psi'\psi'_{xz}\right)+\mathrm{V}\left(\psi'_y\psi'_z-\psi'\psi'_{yz}\right)\right]\end{pmatrix}+\mathrm{C_U M} \tag{2}$$

Where, geostrophic stream function is defined as $\psi=\phi/f$; ϕ, is geopotential and f is the Coriolis parameter with the earth's rotation rate Ω; ψ', a perturbation streamfunction in x, y, z directions; M, phase-independent quantity; p = (pressure/1000 hPa); C_U, the vector that represents the phase propagation in the direction of U; N, the buoyancy frequency. U, the time mean zonal wind; V, the time mean meridional wind. The WAF vector indicates the wave activity direction. A divergent and convergent WAF indicates emitted and absorbed waves, respectively, that is, the amplification and shrinkage of wave activities. A positive vertical WAF represents ascending wave transmission from the lower troposphere.

To identify the covariability relationship among energy transfer terms, surface temperature and atmospheric circulation anomalies, singular value decomposition (SVD) analysis is employed. To quantitatively describe wave pattern, Empirical orthogonal function (EOF) analysis is performed to display the spatial and temporal patterns of the atmosphere (geopotential height and vorticity). A synthesis analysis is applied to show the drought related circulation. The multiscale variability is determined with an adaptive and temporally local filter tool known as ensemble empirical mode decomposition (EEMD, Wu and Huang, 2009). Linear-detrended series is done for exploring annual variability. In addition, other statistical methods are applied, such as Monte Carlo test, correlation analysis, Student's *t*-test, and so on.

Drought is defined as CDDs above the 80th percentile in the base period of the JA precipitation for 55-years from 1961 to 2015, so as to keep at least one case appearing in every year. The selected extreme droughts are defined as CDD frequency higher than twice standard deviation (*SD*) and there are observed drought records. Based on this, many extreme droughts occur after 1997, we will focus on the period after 1997 with successive extremes which considered to occur under the same background (Zhang *et al*., 2019a) to explore causes. Some extreme years with observed drought records are used for contrasting circulation characters, those are 1997, 1999, 2002, 2005, 2006, 2007, 2010, 2012, and 2014.

3 | RESULTS AND DISCUSSION

3.1 | Circulation anomaly and Eurasian wave pattern

Most of the summer climate in NC is dominated by both of the monsoon circulation and the westerly, leading to large variability in the summer precipitation. Given that JA extreme precipitation mainly occur in August which affect water storage (Shen *et al*., 2011; Zhang *et al*., 2019a), therefore, we focus on JA drought and its causes. The anomalous 500-hPa geopotential height and stream field in JA after 1997 is shown in Figure 1. The results show five positive anomalous centres of 500-hPa geopotential heights, including the northwestern Atlantic, northern Europe, southern Lake Baikal, eastern Japan, and eastern Siberia; a negative geopotential height over Eurasia is obvious, and it extends over the Kara Sea and Siberia towards the northwestern Lake Baikal (Zhang *et al*., 2015). At the same time, the anticyclone anomaly over NC corresponds to a weakening in the trough around 120°E and enhancing in the ridge on the southwest of the Lake Baikal; in contrast, a cyclonic anomaly in the mid-high

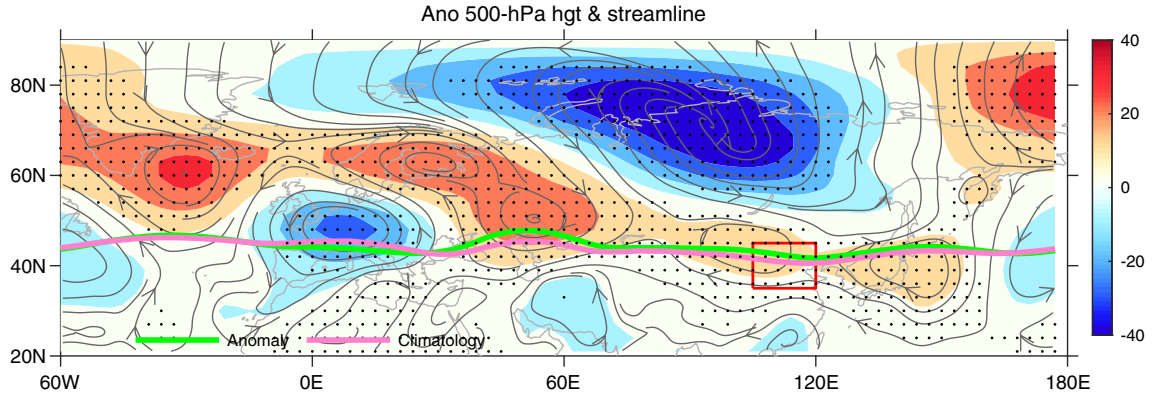

FIGURE 1 Anomalies in 500-hPa geopotential height (gpm, shaded) and streamlines (thin black line); the 5,680-gpm isolines in climatology (pink) and anomaly year (1997–2015, green), respectively. The red box highlights NC. Stippling highlights statistical significance at the 95% confidence level, based on a Student's *t*-test at each grid cell [Colour figure can be viewed at wileyonlinelibrary.com]

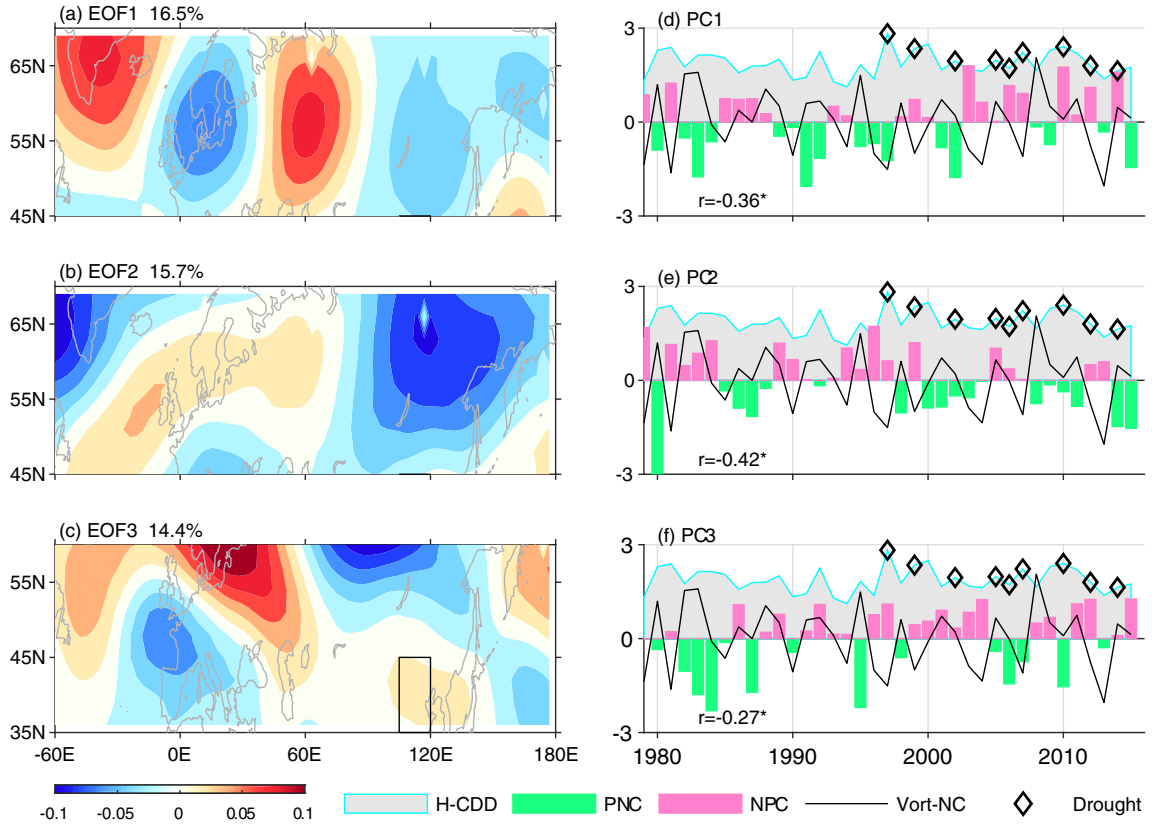

FIGURE 2 The two leading EOFs of the 500-hPa geopotential height anomalies in JA during 1979–2015 over the mid-high-latitude Eurasia (a,b, the third and the fourth pattern, redefined as the first and second pattern in the study), the EOF of the 500-hPa anomaly over the mid-latitude Eurasia (c, the second pattern, redefined as the third pattern in the study), and the normalized leading PCs (bar) and the extreme drought series (H-CDD frequency higher than the 95th percentile) in JA over NC (grey area diagram, d–f). Units are arbitrary. Diamond symbols stand for the selected extreme drought years, with drought frequency higher than double *SD* and observed drought records. All three selected leading patterns have high correlations with the vorticity over NC (Vort-NC, black thick line in d–f). Symbol * in (d–f) notes statistical significance at the 95% confidence level from Monte Carlo simulations. The black box in (c) highlights NC [Colour figure can be viewed at wileyonlinelibrary.com]

latitude is observed over southern China. The circulation anomaly over Eurasian continent also clearly exhibits a wavelike pattern.

To quantitatively describe the wavelike pattern, EOF analysis of the temporal covariance matrix is performed using the 200-hPa geopotential height field and vorticity

in JA. Given that the EU pattern described by the geopotential height is clearer over the high latitudes than that over the middle latitudes, however, the vorticity is clearer over the middle latitudes. Therefore, we perform EOF analysis of the geopotential heights and vorticity separately (i.e., for 45–70°N and 35–60°N).

Firstly, the first six modes of EOF for the geopotential heights over the high latitudes are investigated, which are significantly separated from each other tested by North test, the two modes shown in Figure 2a,b are analysed, because their principal components (PCs, Figure 2d,e) show high correlation with the vorticity anomaly over NC, being responsible for extreme droughts (area chart and diamond marks in Figure 2d,e).

The first EOF mode over the high latitudes clearly exhibits a wavelike structure, which is characterized by a notable Eurasian teleconnection pattern (EU, Wang and Zhang, 2014) that approximately extends across the NA via the western coast of Europe, the Ural Mountains and the Lake Baikal, with a positive anomaly from NA to Greenland and the Ural Mountains, and a negative anomaly over the western coast of Europe and the Lake Baikal. The explained variance rate is 16.5%. The second EOF mode also clearly exhibits a wavelike structure with a positive anomaly extending from NA to the west of Ural Mountains, and a negative anomaly stretching from southern Europe to the Mediterranean Sea and the Lake Baikal to East Siberia. The explained variance rate is 15.7%. The wave pattern is similar to the Eurasian-Pacific teleconnection pattern discovered by Gutzler and Wallace (1981). Although there are low variance rates of both EOF modes, they could explain small probability extremes.

Secondly, the spatial and temporal patterns of vorticity over the middle latitudes (35–60°N, 60°W–180°E) are investigated through EOF analysis. The PC of the vorticity pattern (second pattern, Figure 2c) shows a weak correlation with the vorticity over NC at a 90% confidence level, with the variance of 14.4%. The wave pattern extends across the mid-latitude NA via the west coast of Europe downward to the Caspian Sea, Lake Balkhash, NC, and northeastern Asia. And, it is triggered into the subtropical JS, which is similar to the wave pattern forced by Indian monsoon heating (Enomoto, 2004; Ding and Wang, 2007). These wave patterns are the low-frequency waves upon the quasi-stationary wave, which can lead to magnifying amplitude of quasi-stationary wave due to resonance, and thereby impacts on E–W and N–S locations of quasi-stationary waves linking to extremes (Petoukhov *et al.*, 2013; Zhang *et al.*, 2019a). Therefore, these three low-frequency waves could possibly explain the droughts in NC.

The PCs corresponding to above three EOF modes show increasing trend of the wavelike patterns over the high latitudes with a positive distribution after 1990s, and the decadal abrupt is significant (Figure 2d,e). The PCs exhibit significant negative correlation with the vorticity over NC with correlation coefficients of −0.36, −0.42 and −0.27; these PCs reveal that enhanced low-frequency waves are helpful to magnitude amplitudes of quasi-stationary wave, which are responsible for extreme weather events therein (Petoukhov *et al.*, 2013; Coumou *et al.*, 2014). Therefore, the forcing source of those low-frequency waves is significant for predicting the circulation anomaly and drought in NC, which will be further explored in the next section.

3.2 | Relation of the KE distribution with the Eurasian low-frequency wave pattern

From perspective of energy, the positive KE anomalies can provide energy for the low-frequency wave, it is therefore necessary to address the source. Figure 3a

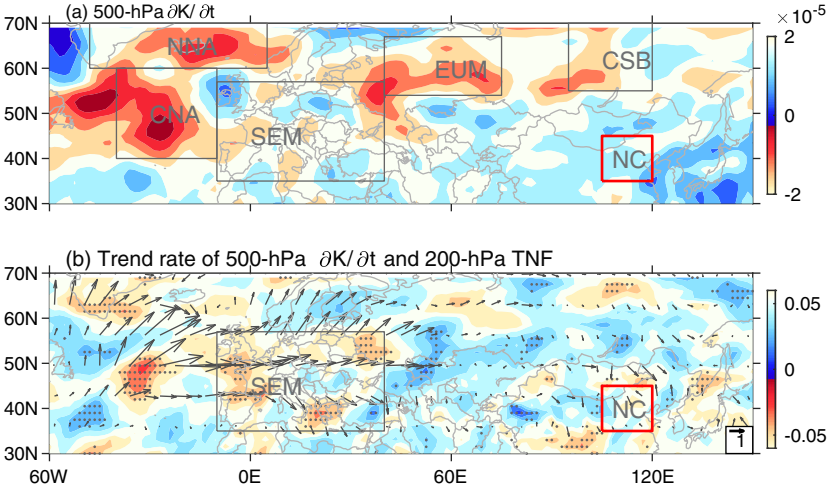

FIGURE 3 The 500-hPa $\partial K/\partial t$ (a, shaded, unit: $m^2\ s^{-2}$), the trend rates of the 500-hPa $\partial K/\partial t$ (shaded) and the 200-hPa wave activity flux defined by Takaya and Nakamura (b, arrow, TNF) in JA. The black boxes highlight the domains for the positive $\partial K/\partial t$ and its trend rate, stand for five key regions. The red box and stippling is similar with Figure 1 [Colour figure can be viewed at wileyonlinelibrary.com]

shows the distribution of the ∂K/∂t at 500 hPa in JA. There are five positive centres over the extratropical NA and Eurasian continent: (1) the high-latitude North Atlantic to the east of Greenland (defined as NNA), (2) the central North Atlantic (CNA), (3) southern Europe and the Mediterranean Sea (defined as *SEM*), (4) the region to the east of the Ural Mountains (EUM), and (5) Central Siberia to the north of Lake Baikal (defined as CSB). An increasing trend in the ∂K/∂t also occurs over these five regions. Besides, the increasing trend over three other regions, namely, the southern Tibetan Plateau, NC (red box in Figure 3) and Japan, are also significant. Positive KE and increasing KE explains an increase in the blocking over western Russia in many models, particularly in the summertime (Dunn-Sigouin and Son, 2013; Masato *et al*., 2013). Therefore, these five regions are the potential sources of energy transfer, whether it is related to internal variability or other forcing should be further explored.

To interpret the relation between the positive KE anomalies over these regions and the wavelike structures presented in Figure 1, the WAF at 200 hPa is shown in Figure 3b. It reveals two key regions with divergent WAF, one is over the CNA and another is over *SEM*, they are the primary sources of the WAF, which corresponds to ascending vertical WAF in the lower-middle troposphere (Zhang *et al*., 2019a); however, divergent WAF over the other three regions are weaker. The WAF indicates two branches of energy dispersion. One branch is over the high latitudes via northern Europe, the region to the east of the Ural Mountains and Central Siberia, and it is trapped along the subpolar JS and is close to two high-latitude patterns in Figure 2a,b. The other branch of energy dispersion is located along the subtropical JS and is close to the mid-latitude pattern in Figure 2c. These two branches of energy dispersion are responsible for the low-frequency wave behaviours, which ultimately depend on the wave-guiding ability of the JS, influenced by the JS position, width and speed (Manola *et al*., 2013). Due to the energy dispersion along subpolar JS and the energy sinking to the east of the Ural Mountains, the blocking around the Ural Mountains may change more actively in the future, which is also revealed by diabatic processes triggered by warmer SSTs (Croci-Maspoli and Davies, 2009). The energy dispersion over Central Siberia could be transported southward and sank over NC, thereby directly leads to the wave and vorticity anomalies, and it could interpret the relation between the high-latitude wave pattern and the climate anomaly over NC.

To explore how the positive KE anomalies over these five energy regions impact low-frequency waves, the multiscale relations of the ∂K/∂t over those five regions with multiscale PCs of the three wave patterns are analysed by using the EEMD method. The variables with 95% confidence level of correlations are shown in Figure 4. The PC1 exhibits a good correlation with the ∂K/∂t over the region of the NNA on the interannual and interdecadal scales. The PC2 exhibits a good relationship with the ∂K/∂t over the CNA and the *SEM* on the interannual scale, but it also has a high correlation over the *SEM*, the EUM and the CSB on the inter-decadal scale. The PC3 has high correlations with the ∂K/∂t over the four regions except the EUM on the interannual scale and the CNA on the inter-decadal scale. On the multidecadal scale, the ∂K/∂t over all five regions show high correlations with the PC1; the ∂K/∂t over three continental regions show high correlations with PC2; and the ∂K/∂t over four regions except *SEM* show high correlations with the PC3. Figure 4 illustrates the multiscale relations between the ∂K/∂t over those five regions and three dominant patterns; through those wave patterns, an increase in the KE over those regions could modulate multi-scale climate over NC. Thus, the causes of increasing ∂K/∂t are significant for exploring mechanism of the low-frequency wave.

3.3 | The contributions of energy transfer terms

To investigate the cause of the low-frequency wave, the physical mechanisms of the energy transport and transfer terms in Equation (1) are explained, and the corresponding variables of the regional mean and synthesis after 1997 are shown in Figure 5. The variables in the lower troposphere (1000–700 hPa) and in the middle troposphere (600–500 hPa) are contrasted. Over *SEM* (a1,a2), the positive contributions of KE originate from all the energy transfer terms in the lower and middle troposphere in the climatological and drought years, and the major energy transfers are from basic flow (K_m) and buoyancy conversion (B). In drought years, the energy transfers from basic flow (K_m), buoyancy conversion (B) and vertical KE flux (Q_k) are higher than climatology, contributing to the increasing KE.

As for the EUM (b1-b2), the positive energy transfers are from basic flow (K_m) and pressure flux (Q_p) in the lower and middle troposphere, and they are the primary contributions. In drought years, pressure flux (Q_p) and buoyancy conversion contribute to decreasing KE.

As for CSB (c1,c2), the positive contributions for KE are from basic flow (K_m) and pressure flux (Q_p) in the lower and middle troposphere, and the primary contributions are from basic flow (K_m). In drought years, basic flow (K_m) and decreasing friction and divergence (D) contribute to increasing KE.

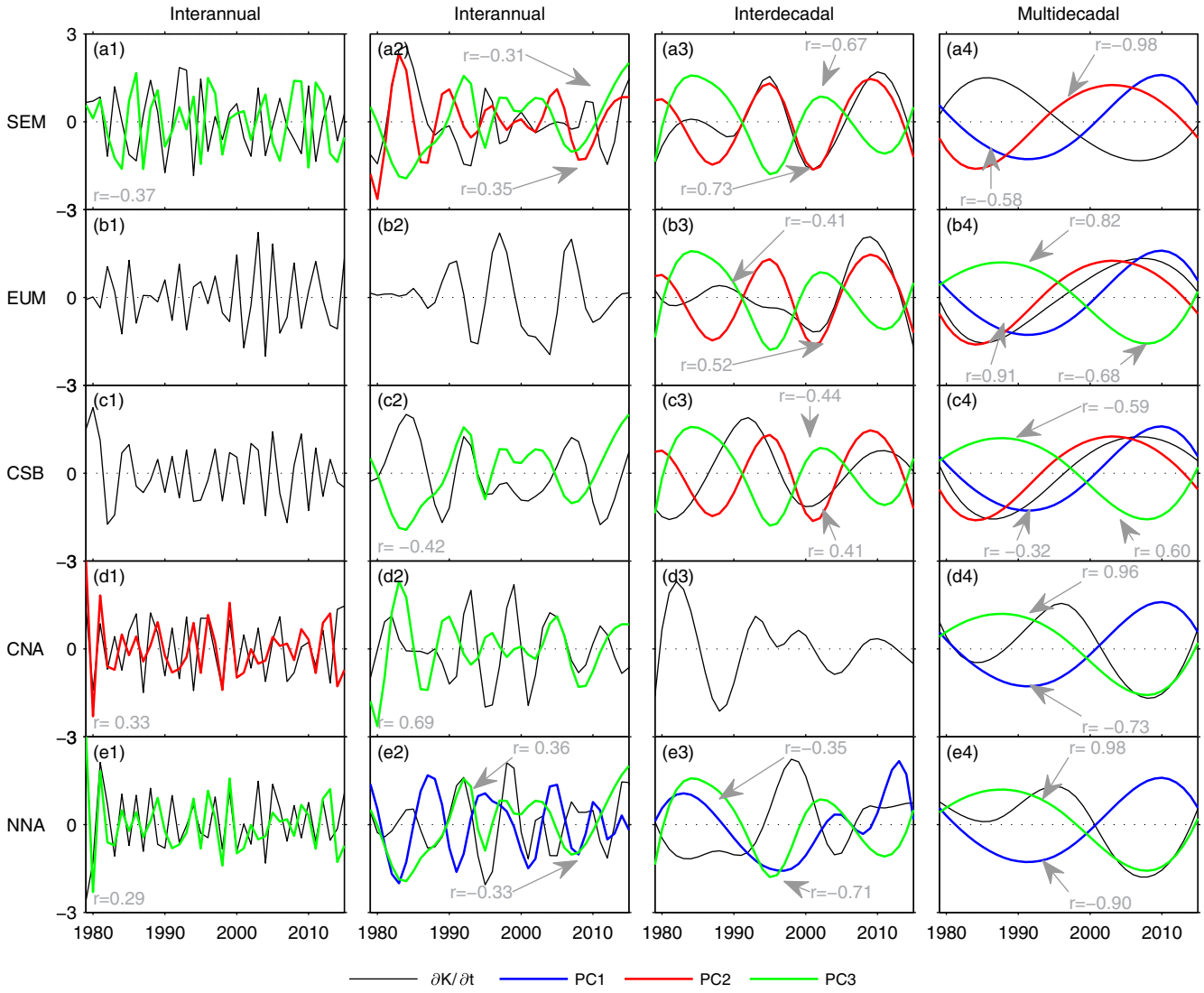

FIGURE 4 The temporal series of standardized multiscale PCs (colour line) and 500-hPa $\partial K/\partial t$ (black line) over five key regions, and the four major timescales are determined by the EEMD filter. The four timescales include a 2–3-year interannual scale (a1–e1), a 4-5-year interannual scale (a2–e2), an inter-decadal scale (a3–e3), and a multidecadal scale (a4–e4). Correlation value highlights statistical significance at the 95% confidence level from Monte Carlo simulations. The colour lines of blue, red and green correspond to the multiscale PC1, PC2, and PC3 [Colour figure can be viewed at wileyonlinelibrary.com]

For the CNA (d1,d2), all the energy transfer terms in the lower and middle troposphere are available for KE, and the primary contributions are from basic flow (K_m) and buoyancy conversion (B). In drought years, the main energy transfers are from basic flow (K_m), buoyancy conversion (B), and vertical KE flux (Q_k).

For the NNA (e1,e2), the positive energy transfers are from eddy (K_s) and pressure flux (Q_p) in the middle and lower troposphere, and many terms are negative in climatological and drought years, the relationship between KE and the frictional and subgrid-scale effects is ignored in the study.

By contrasting these energy transfer terms, we find that the energy transfer from basic flow (K_m) is the primary contributions over four of the key regions (i.e., except for the NNA), especially in the middle troposphere, indicating interactions between the waves and basic flow. In addition, the positive KE flux (Q_k) is larger in the lower troposphere over CNA and *SEM*, which contribute to the ascending KE transfer. The positive energy buoyancy conversion (B) in the lower troposphere reveals an increasing baroclinicity contribution to the KE, which is possibly related to the boundary layer turbulence (Liang, 2016; Zhang *et al*., 2019a; Zhang *et al*., 2019b).

To further show the spatial relation of ∂K/∂t and the related energy transfer terms, the first SVD mode of them is analysed. On the annual scale (Figure 6), the ∂K/∂t exhibits a high-latitude wave pattern with a consistent

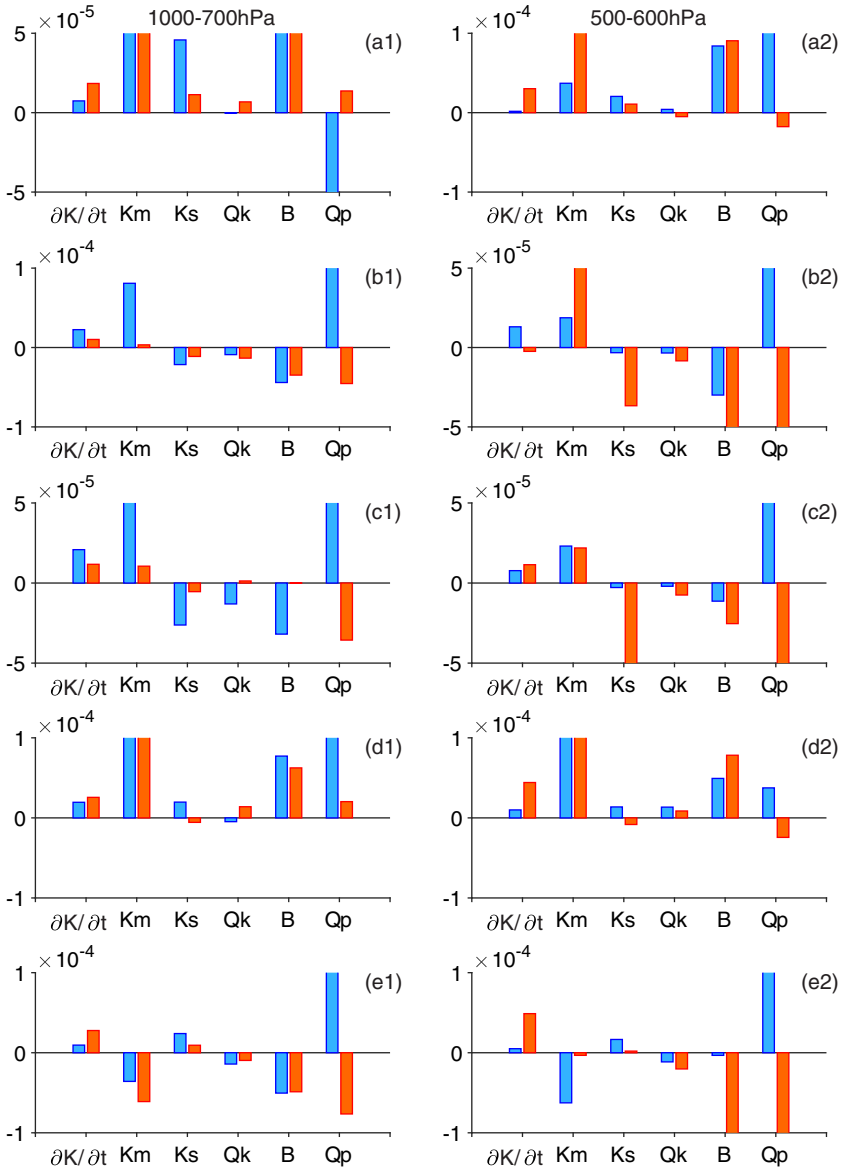

FIGURE 5 The JA climatological (blue, unit: $m^2\ s^{-2}$) and anomalous years (red, after 1997, unit: $m^2\ s^{-2}$) $\partial K/\partial t$ and the related energy transfer terms at 700 hPa (a1–e1) and 500 hPa (a2–e2) over the *SEM* (a1,a2), EUM (b1,b2), CSB (c1,c2), CNA(d1,d2), and NNA(e1,e2). $\partial K/\partial t$ is the rate of KE variation; K_s is the energy transfer from the high-frequency eddy; K_m is the energy transfer from basic flow; Q_k is the vertical KE flux; Q_p is the rate of KE caused by pressure gradient force; and B is the rate of buoyancy conversion [Colour figure can be viewed at wileyonlinelibrary.com]

trend over the NA, southern Europe, Central Asia, and around Lake Baikal; moreover, it is inconsistent with the variation over northern Europe and around the Ural Mountains (a). The energy transfer from basic flow shows a consistent relationship with the ∂K/∂t over *SEM*, the NNA, and the region to the northwest of the CNA (b). The energy transfer from eddy shows a consistent relationship with the ∂K/∂t over part of *SEM* and the EUM (c). The energy from the buoyancy conversion shows a consistent relationship with the ∂K/∂t over part of *SEM* and the NNA (d). These consistent relations agree with the results from Figure 5. The increasing KE reveals that the *SEM*, the CNA, and the NNA are key centres related to the energy transfer from the basic flow and eddy, as well as buoyancy conversion on the annual scale.

On the decadal scale (Figure 7), the ∂K/∂t in most of the regions exhibit consistent trends, especially over the NA, the Ural Mountains and Siberia, which are different from other European regions (a). The energy transfer from basic flow shows a consistent relationship with the ∂K/∂t over four of the key regions, namely, the CNA, *SEM*, EUM, and CSB (a,b); however, it shows the reverse relationship with ∂K/∂t over the NNA. The energy transfer from basic flow exhibits a NW-SE pattern with a meridional-zonal shift that is closely related to the ∂K/∂t over *SEM* and the CNA. The energy transfer from eddy shows a consistent relationship with the ∂K/∂t over the north of *SEM* and the region to the southwest of the CNA (c). The buoyancy conversion shows a consistent relationship with the ∂K/∂t over the east of the CNA and the south of *SEM* along the east coast of NA in addition to the CSB (d).

These energy transfers from eddy and basic flow and the buoyancy conversion over *SEM* and CNA are also

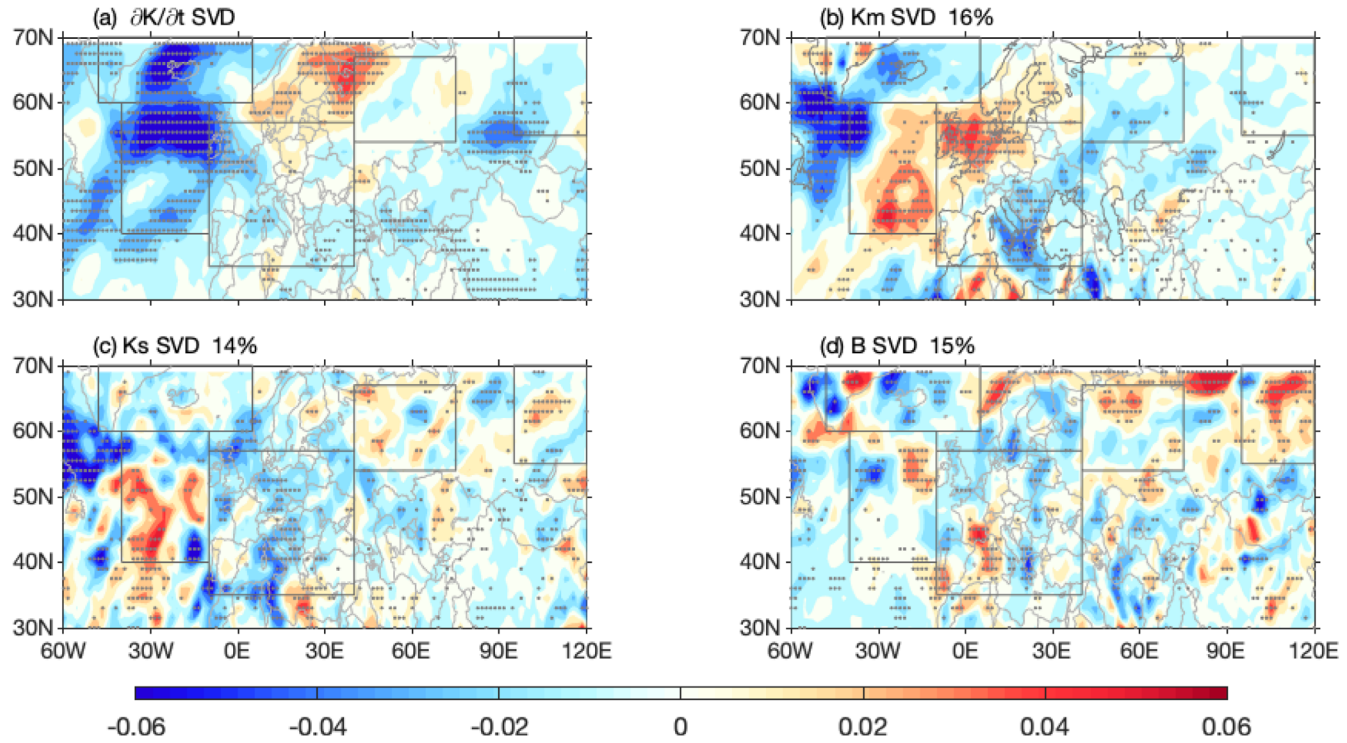

FIGURE 6 Singular vectors pattern of the first SVD mode for the $\partial K/\partial t$ (a) and the related terms (b–d) at 500 hPa over the North Atlantic and mid-latitude Eurasia on the annual scale. This mode accounts for 14–16% of the squared covariance fraction (SCF). Stippling is similar with Figure 1. The black box domains are the same as which in Figure 3. $\partial K/\partial t$ and the related terms are the same as Figure 5 [Colour figure can be viewed at wileyonlinelibrary.com]

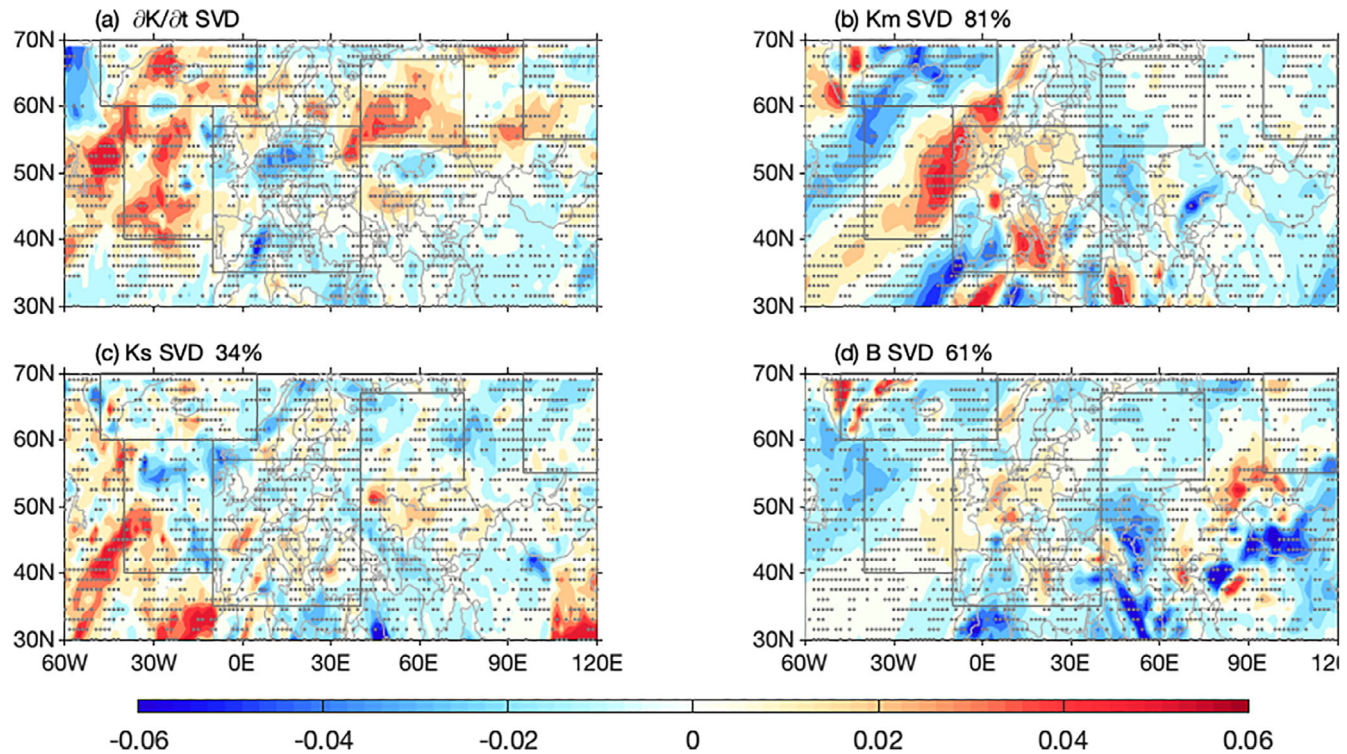

FIGURE 7 Singular vectors patterns of the first SVD mode for the $\partial K/\partial t$ (a) and the related terms (b–f) at 500 hPa over the North Atlantic and the mid-latitude Eurasia on the decadal scale. This mode accounts of 55, 81, 34, and 61% for SCF. Stippling, black box domains and $\partial K/\partial t$ and the related terms are the same as Figure 6 [Colour figure can be viewed at wileyonlinelibrary.com]

consistent with the KE and increase KE on the decadal scale. These terms contribute to both of the high-latitude and the mid-latitude wavelike pattern shown in Figure 2c. Therefore, the CNA and *SEM* are two key sources for decadal anomaly of the low-frequency waves, which could interpret the decadal correlation in Figure 4a3,a4,d4. However, energy transfer from the eddy shows an inconsistent relationship with the ∂K/∂t over EUM and CSB, which indicates that the KE can be converted into eddy, and it agrees with the result from Figure 5b,c. The energy transfer from basic flow and buoyancy conversion over the CSB converted into KE could enhance the meridional circulation and energy transport over the CSB and thereby impact on circulations and extreme climate over NC.

3.4 | The mechanism of the KE anomaly

3.4.1 | The impact of the jet stream anomaly

Among the energy transfer terms, it is clear that the energy transfer from basic flow contribute to major KE, especially over the *SEM* and the CNA, which is related to the anomaly of basic flow that could be represented by the westerly JS and zonal wind. Therefore, it is important to understand the reason why the energy transfer from basic flow contributes to the large variability in the KE in recent two decades.

Figure 8a1-a2 shows the SVD of the zonal wind at 200 hPa and the energy transfer from basic flow (K_m). The zonal wind distribution at 200 hPa is similar to that at 500 hPa; the zonal wind mode shows a JS-like distribution, and it indicates a W-E and N-S shift of the NA JS, North African JS and Asian JS. Previous studies show that the zonal wind reveals an N-S shift in the NA JS with a positive/negative NAO (Luo *et al*., 2007). Both the N-S shift and the W-E extending of the NA JS change with global warming, exhibiting an anomaly basic flow, which is identified to link to NA and Eurasian continent (Woollings and Blackburn, 2012; Zhang *et al*., 2019a). Besides, the positive AMO since the mid-1990s can cause SRP-like atmospheric anomalies(Zhang *et al*., 2020), and result in Eurasian summer nonuniform warming, which could have important effect on the wave patterns and KE.

The zonal wind is consistent with the energy transfer from basic flow over the four regions except the NNA, especially over the CNA and *SEM*. Based on this, the eastward extension of the NA JS and the northward shift of the North African JS could increase the basic flow and the energy transfer from basic flow over the CNA and *SEM*, which could be used to interpret a positive KE.

To explore the interannual relations between zonal wind and the energy transfer from basic flow (K_m), the SVD of linear detrended pattern is analysed. The first mode of detrended zonal wind exhibits both N-S and W-E extension (Figure 8, b1-b2), and it corresponds to the N-S shift and the W-E shift of the North African JS and NA JS. The southeastern shift in the NA JS corresponds to the consistent pattern with the detrended energy transfer from basic flow over the region to the west of the CNA and most of *SEM*. However, the northward shift in the North African JS corresponds to a consistent pattern of the detrended energy transfer from basic flow over the *SEM*. As shown in Figure 8c1,c2, the PC time series of the first SVD mode shows the same trend of the zonal wind and the energy transfer from basic flow, with close to a 100% correlation for those without detrended analysis. The correlation of the detrended zonal wind and the energy transfer from basic flow is 32%.

3.4.2 | The impact of baroclinicity

The parameter $-\frac{\partial U}{\partial P}$ represents the vertical zonal-wind shear, which could indicate the baroclinic instability. The larger the vertical wind shear is, the higher the baroclinic instability, and the more corresponding the vertical Q_k is. The $-\frac{\partial U}{\partial P}$ and Q_k from 850 hPa to 500 hPa are shown in (Figure 9). Both of $-\frac{\partial U}{\partial P}$ and Q_k exhibit significant positive correlations over *SEM* and CSB, with 95% confidence level, and it facilitates the ascending KE flux to the upper troposphere with an increase in the horizontal and vertical wind shear, it is in accordance with increasing Q_k in drought years in Figure 5. However, the correlations of $-\frac{\partial U}{\partial P}$ and Q_k are weak over NNA, CNA, and EUM.

3.4.3 | The impact of the surface temperature

The above results show that the energy transfer from the eddy, the energy buoyancy conversion and the KE flux (Q_k) in the lower troposphere are larger than those in the middle troposphere, and the KE has a more significant variation. Thus, we should address the actual cause of the KE conversion and three energy transfer terms in the lower troposphere.

Coincident with global warming, the surface thermal anomaly over the mid-high latitudes exhibits significant variability, which is associated with the circulation anomaly (Dong *et al*., 2017). To determine the impact of the surface temperature on the KE conversion, the first SVD mode of the detrended surface temperature (T_s) and the key energy transfer terms are investigated, the energy transfer terms

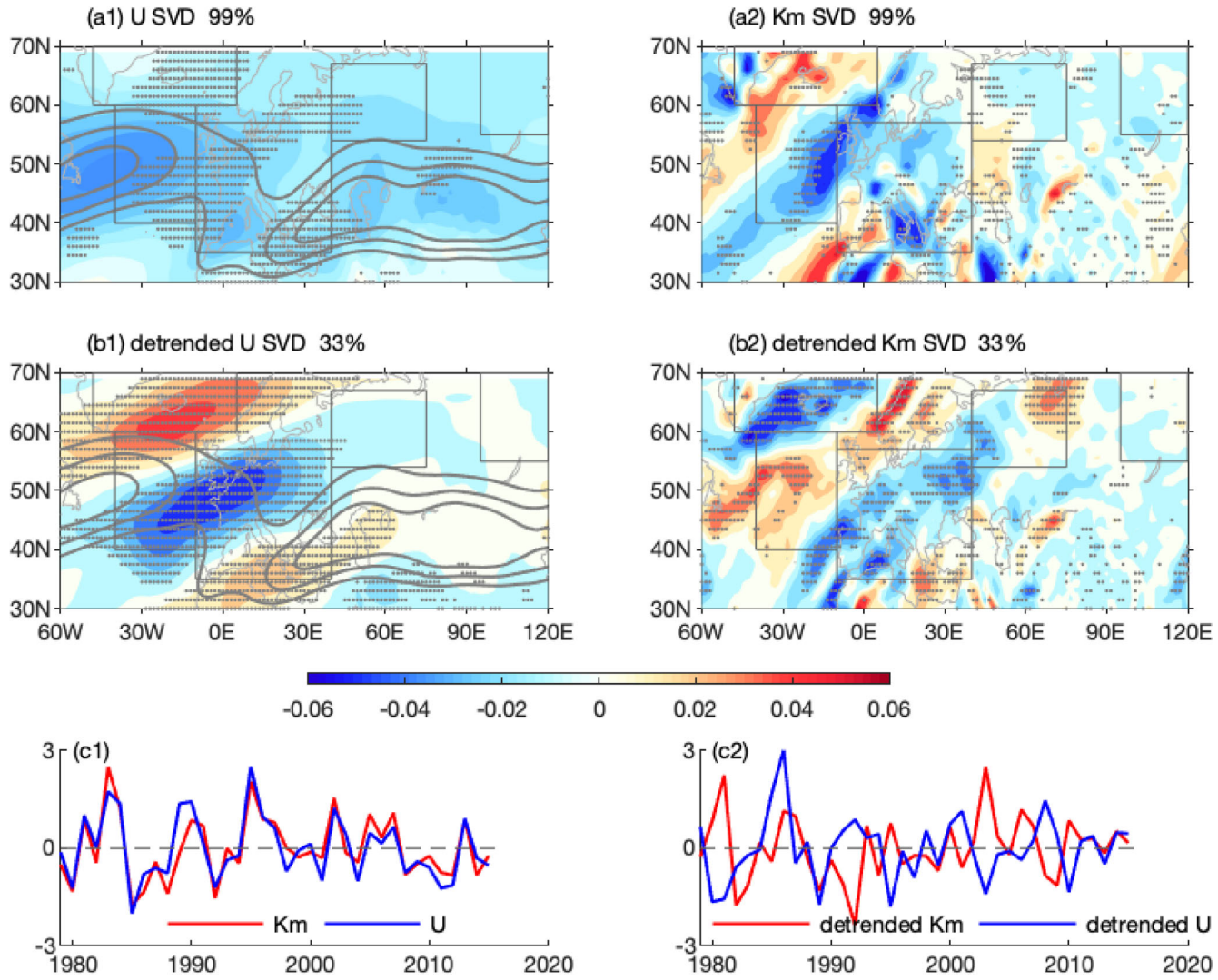

FIGURE 8 Singular vectors pattern of the first SVD mode for the zonal wind U (a1) and the energy transfer from basic flow (K_m, a2), the detrended U (b1) and detrended K_m (b2) at 500 hPa. Times series of associated PCs are in lines (c1,c2). This mode accounts for SCF of 99 and 33%. The thick pink contour (a1–b1) is climatological 200-hPa zonal wind (U = 15, 20, 25 m/s). Stippling and black box domains are the same as Figure 6 [Colour figure can be viewed at wileyonlinelibrary.com]

include the buoyancy conversion (Figure 10a1,a2), baroclinity related factor, Q_P (Figure 10b1,b2) and the energy transfer from the eddy (Figure 10c1,c2), are investigated.

The first SVD mode of the detrended surface temperature and the 700-hPa buoyancy conversion indicates that the annual surface temperature exhibits a wavelike pattern with negative anomalies over northern Europe and from the Lake Baikal to NC, and significant positive anomalies from the EUM to the CSB, the *SEM* to Central Asia and Greenland. The buoyancy conversion is consistent with the surface temperature over those key regions. The result indicates that the boundary turbulence and baroclinic instability increases with an increase in the surface temperature over *SEM* and Greenland, which favours for buoyancy conversion, with the explained variance of 23%.

The first SVD mode of the detrended surface temperature and pressure flux Q_p (c,d) indicates that the annual surface temperature exhibits a positive anomaly over the CSB and *SEM* and a negative anomaly over the Central Asia, the CNA, and NNA. The contribution of the pressure flux shows a consistent distribution over the region to the east of the CNA, the part of *SEM* and NNA; the explained variance is 74%. The pressure flux is caused by a pressure gradient force, which indicates that the pressure gradients over those regions increase with the increase of the surface temperature and baroclinicity instability, finally resulting in a high-pressure flux and a mid-upper KE, especially over the east coast of NA and the east of Greenland and NNA.

The first SVD mode of the detrended surface temperature and the energy transfer from the eddy (K_s) is

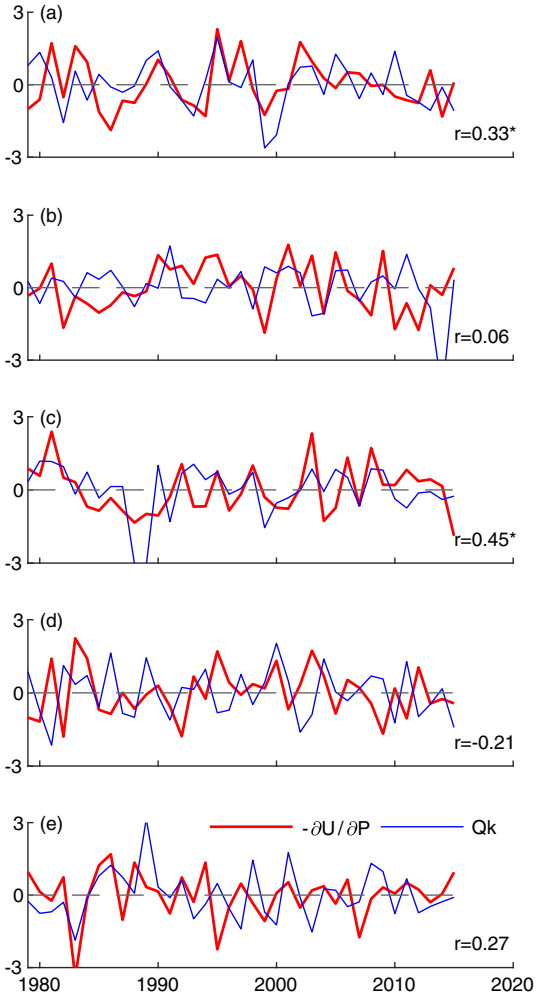

FIGURE 9 Time series of standardized $-\frac{\partial U}{\partial P}$ and the vertical KE flux (Q_k) from 850 hPa to 500 hPa and their correlations over *SEM* (a), EUM (b), CSB (c), CNA (d), and NNA (e), "*" notes statistical significance at the 95% confidence level [Colour figure can be viewed at wileyonlinelibrary.com]

showed in Figure 10c1,c2, the energy transfer from the eddy exhibits a reverse distribution with the surface temperature, except for the North Europe, East Asia and Tibetan Plateau, the explained variance is 27%, which indicates that increase in the surface temperature leads to the energy transfer from KE to the eddy over these three regions, favouring for eddy development.

The above results show that the vertical wind shear and JS anomaly are closely related to the KE, and surface temperature constitutes the local forcing on the buoyancy conversion, pressure flux and part of the eddy increasing in the lower troposphere, thereby reflecting the effect of the boundary layer and the increasing instability. These result in positive KE, which could develop and strengthen the low-frequency waves. This finding differs from those of previous studies (Hoskins and Karoly, 1981). In general, Rossby waves are triggered much more readily by deep convection in the lower-latitude rather than by mid-higher-latitude boundary layer processes (Hoskins and Karoly, 1981). In accordance with this conclusion, except for the effect of global warming, surface temperature is partly linked to the lower-latitude forcing. Sato *et al.* (2014) also indicated that a Rossby wave train originated over the Gulf Stream, that warmed the Barents-Kara Sea through downward surface heat fluxes and then arched south, leading to a high pressure over Eurasia. However, because of the memory effect of the soil heat capacity on the atmosphere and the feedback, boundary layer forcing could lead to KE variation that modulates the effect of the lower-latitude forcing on the mid-latitude low-frequency waves.

3.5 | KE transport along the subtropical JS

Above results reveal that the CNA and Europe are two sources of increasing KE, which excite and enhance the low-frequency wave, so as to further identify the contribution of increasing KE over these sources to the low-frequency wave, the energy transport is further investigated. Figure 11 shows climatic change trend of 200-hPa ∂K/∂t (a), zonal advection (b) and meridional advection of KE (c) and zonal wind (15, 20, 25 m/s). The results further identify the increasing KE, which mainly appear at the exit of NA JS. In addition, the positive advection of zonal and meridional KE mainly appears from the exit of NA JS to the entrance of Afro Asian JS, which indicates increasing energy transport and the low-frequency wave triggered into Afro Asian JS (see red arrow), which could influence downward circulation with energy dispersion. The energy transport is the cause of enhancing in the mid-latitude low-frequency wave, which could explain climate anomaly and drought over NC. The increasing energy transport relates to northwestern shift in the Afro Asian JS, which is related to non-uniform zonal warming according to the principle of thermal wind and negative NAO (Woollings and Blackburn, 2012).

3.6 | Simulation of the surface warming effect on KE and low-frequency waves

To reveal the significant effect of boundary forcing on the KE and low-frequency waves over the upper troposphere, the study selected the *SEM* region to simulate the diabatic forcing with climate warming. The forcing of

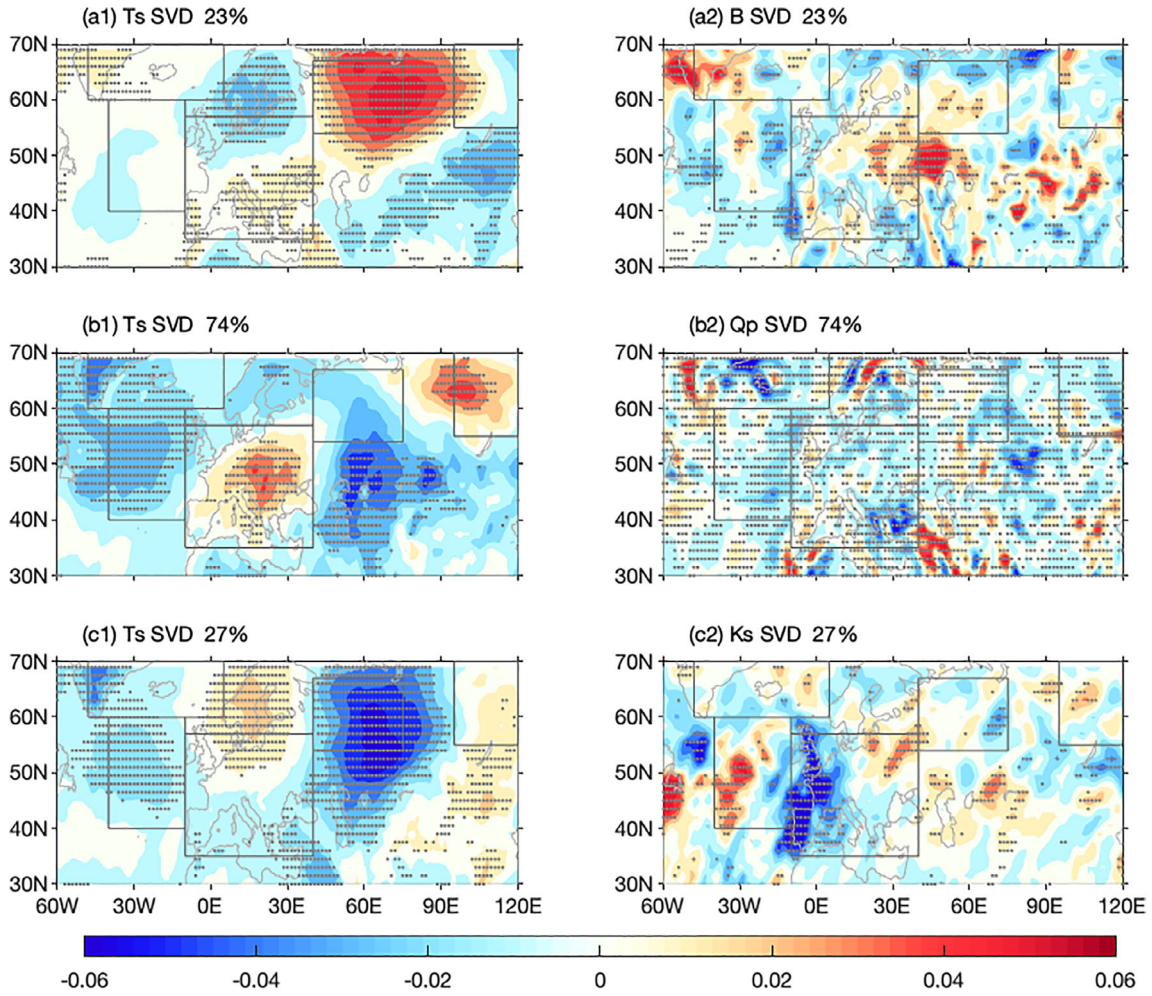

FIGURE 10 Singular vectors pattern of the first SVD mode for the detrended surface temperature (a1–c1) and the 700-hPa buoyancy conversion (B, a2), the contribution of the pressure flux (Q_P, b2), and the energy transfer from the eddy (K_s, c2) over the North Atlantic and the mid-latitude Eurasia. Stippling, black box domains and KE related terms are the same as Figure 6 [Colour figure can be viewed at wileyonlinelibrary.com]

diabatic heating was performed by the LBM with a position in Europe (centre: 47°N, 20°E) at 700 hPa, with an initial heating intensity of 6 K/day, and a horizontal scale of 12° × 6°. The anomaly distributions of the geopotential height and wind velocity are analysed (Figure 12), and the positions of the climatological and simulated zonal wind equal to 20 m/s at 200 hPa are contrasted, to reveal the boundary warming effect on the energy transfer from basic flow to the KE.

The simulation of the increasing diabatic heating with the increasing temperature over Europe indicates two significant wave patterns over the mid-latitudes and high latitudes, both of which are linked to an anticyclone anomaly over NC; in addition, a 20-m/s zonal wind exhibits a decrease from Central Asia to the southern Mediterranean Sea and northern Africa, indicating a shrinking in the subtropical Afro Asian JS. However, there is an increase in the 20-m/s zonal wind over Europe and the eastern coast of the NA exhibiting a northward shift in the entrance of the Afro Asian JS and the eastward extension of the NA JS, which is helpful to the energy transfer from basic flow to KE. Moreover, the increasing in surface warming of Europe and the Mediterranean Sea facilitates the energy transfer and increase KE transport, favouring the development and enhances of three low-frequency wave patterns, as well as association with extremes. The simulation results agree with above diagnostic analysis, with clear wave pattern described by geopotential height and wind velocity.

4 | CONCLUSION

By using the localized multiscale energy and vorticity analysis and the WAF, the study reveals the energy transfer processes and forcing sources, and the LBM is used

for sensibility experiment to identify the forcing and physical processes. The study implies that external forcing of the mid-latitude NA and continental diabatic heating are important in determining the statistical features of anomalous quasi-stationary waves, that is, the low-frequency wave effect on the circulation, which should be considered in evaluation and prediction of extratropical extremes.

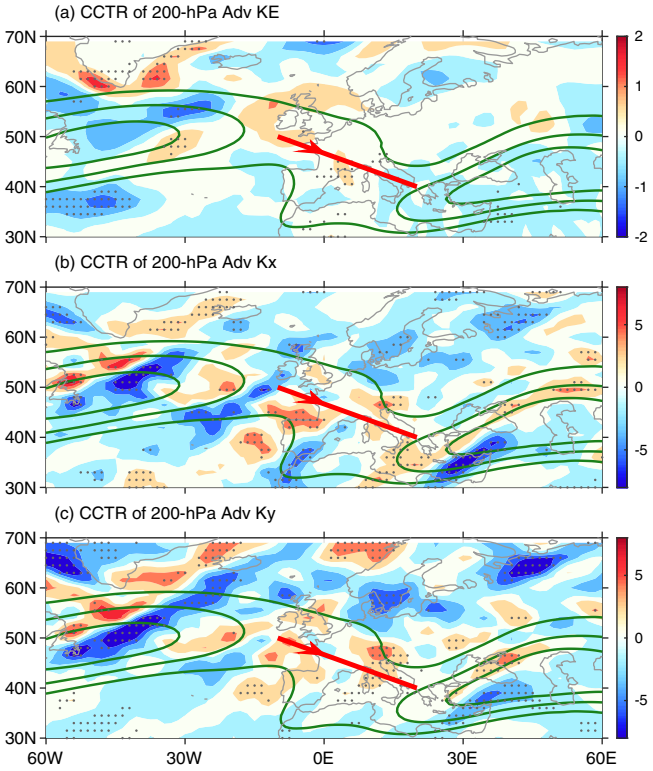

FIGURE 11 Climatic change trend of 200-hPa $\partial K/\partial t$ (a, 10^{-4} m^2s^{-2}/10a, shaded), zonal advection of kinetic energy (b, shaded, 10^{-4} m^2 s^{-2}/10a), meridional advection of kinetic energy (c, shaded, 10^{-4} m^2 s^{-2}/10a), and climatological 200-hPa U = 15, 20, 25 m/s), red arrow exhibits direction of kinetic energy transport. Stippling is similar with Figure 1 [Colour figure can be viewed at wileyonlinelibrary.com]

An analysis of WAF revealed the eastward propagation of three wave patterns: two wave patterns start over the NA, Europe and Mediterranean Sea, and pass the Ural Mountains and Siberia before propagating southward to NC; another pattern passes NC and northeastern Asia via Central Asia and the northern flank of the Tibetan Plateau.

This paper determines all of the energy transfer terms quantitatively to delineate the energy transport and transfer processes, which could reflect the forcing sources, where wave energy sinks and where the circulation is anomalous. Thus, the sources of KE and their importance can be identified. The method we used covers all spatial scales, and transition between different scales. The anomaly of the wave pattern is strengthened by the positive KE, especially over the central of NA and Europe. The KE is contributed by the energy transfer from basic flow, which is possibly related to JS position, the northwestern shift in the entrance of the Afro Asian

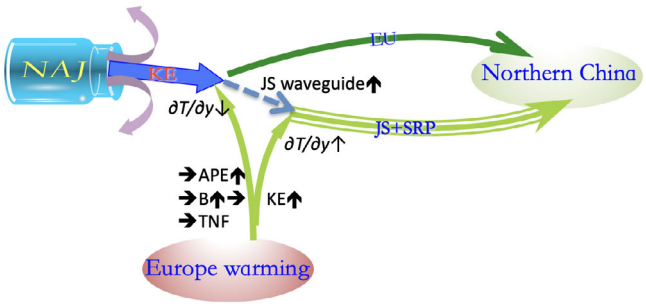

FIGURE 13 Schematic diagram summarizing the physical processes of Europe surface warming and North Atlantic SST pattern effect on jet stream (JS) and baroclinicity, leading to seasonal kinetic energy (KE) conversion, and the relation with the low-frequency waves (EU, SRP) imposed on the amplitude of quasi-stationary waves, influencing Northern China drought. NAJ: North Atlantic jet; B: baroclinic energy conversion to seasonal KE; TNF: wave activity flux defined by Takaya and Nakamura (2001); $\partial T/\partial Y$: zonal temperature gradient [Colour figure can be viewed at wileyonlinelibrary.com]

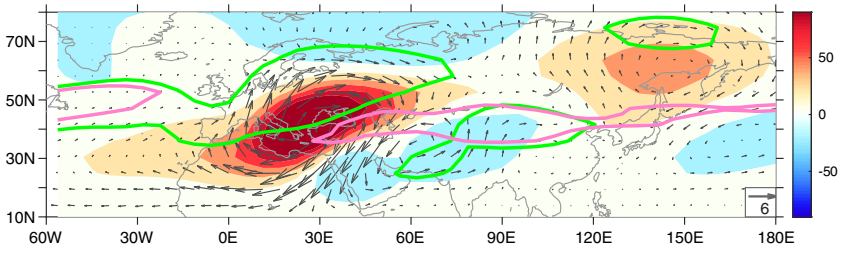

FIGURE 12 Simulation anomalies of the geopotential height (shaded, gpm) and wind velocity (arrows) with diabatic heating, climatological U = 20 m/s (pink lines) and simulated U = 20 m/s (green lines) at 200 hPa; the forcing is over Europe (centre: 47°N, 20°E) at 700 hPa with an initial heating intensity of 10 K/day (horizontal scale: 12°E × 6°N) [Colour figure can be viewed at wileyonlinelibrary.com]

JS and the southeastern extension of the exit of the NA JS. Some energy terms over the lower troposphere are larger than those over the mid-upper troposphere; they include the buoyancy conversion and vertical energy flux, that is related to the boundary thermal forcing, leading to an increase in the baroclinicity and the mid-upper-troposphere KE, as well as magnitudes of temperature anomaly (Schneider *et al*., 2015). In addition, northwestern shift in the entrance of Afro Asian JS enhances JS waveguide ability and strengthens the mid-latitude wave trains (Figure 13).

Besides NA and continental forcing effect on the quasi-stationary waves, warm winters over northwestern Canada and Greenland corresponding to the positive NAO disturbs the quasi-stationary waves propagating from the tropical North Pacific (Ding *et al*., 2014); the Arctic amplification related heat flux impacts the low-frequency wave pattern on an intra-seasonal timescale, which is associated with enhanced Indian Ocean convection (Lee *et al*., 2011), Han *et al*. (2018) also revealed that both tropical Indian Ocean SST and Mediterranean Sea to Central Asia enhance a southern Eurasian wave train extending eastward and affect Japan (Sato and Takahashi, 2006). Those forcing related wave patterns are closely linked to the development of the blocking high over northern Europe and Ural Mountain, and anomalies of quasi-stationary waves (e.g., Scaife *et al*., 2010; Schubert *et al*., 2014). Those forcing are important for extremes.

ACKNOWLEDGEMENTS

This research was jointly supported by the National Key R&D Program of China (Grant No. 2018YFC1507101), the National Natural Science Foundation of China for Key Program (Grant No. 41975083) and by the Priority Academic Program Development of the Jiangsu Higher Education Institutions (PAPD). The authors would like to thank the ECMWF for providing the ERA-interim data (http://apps.ecmwf.int/datasets/).

ORCID

Jie Zhang https://orcid.org/0000-0002-9204-9834

REFERENCES

Ambrizzi, T., Hoskins, B.J. and Hsu, H.H. (1995) Rossby wave propagation and tele-connection patterns in the Austral winter. *Journal of the Atmospheric Sciences*, 52, 3661–3672.

Chen, H., Teng, F., Zhang, W. and Liao, H. (2017) Impacts of anomalous mid-latitude cyclone activity over East Asia during summer on the decadal mode of East Asian summer monsoon and its possible mechanism. *Journal of Climate*, 30 (2), 739–752.

Coumou, D., Petoukhov, V., Rahmstorf, S., Petri, S. and Schellnhuber, H.J. (2014) Quasi-resonant circulation regimes and hemispheric synchronization of extreme weather in boreal summer. *Proceedings of the National Academy of Sciences*, 111 (34), 12331–12336.

Coumou, D. and Rahmstorf, S. (2012) A decade of weather extremes. *Nature Climate Change*, 2(7), 491–496.

Croci-Maspoli, M. and Davies, H.C. (2009) Key dynamical features of the 2005/6 European winter. *Monthly Weather Review*, 137, 644–678.

Cui, Y., Duan, A., Liu, Y. and Wu, G. (2015) Interannual variability of the spring atmospheric heat source over the Tibetan Plateau forced by the North Atlantic SSTA. *Climate Dynamics*, 45(5–6), 1617–1634.

Dee, D.P., Uppala, S., Simmons, A., Berrisford, P., Poli, P., Kobayashi, S., Andrae, U., Balmaseda, M., Balsamo, G., Bauer, P., Bechtold, P., Beljaars, A.C.M., van de Berg, L., Bidlot, J., Bormann, N., Delsol, C., Dragani, R., Fuentes, M., Geer, A.J., Haimberger, L., Healy, S.B., Hersbach, H., Hólm, E. V., Isaksen, L., Kållberg, P., Köhler, M., Matricardi, M., McNally, A.P., Monge-Sanz, B.M., Morcrette, J.J., Park, B.K., Peubey, C., De Rosnay, P., Tavolato, C., Thépaut, J. and Vitart, F. (2011) The ERA-Interim re-analysis: configuration and performance of the data assimilation system. *Quarterly Journal of the Royal Meteorological Society*, 137, 553–597.

Ding, Q., Wallace, J.M., Battisti, D.S., Steig, E.J., Gallant, A.J., Kim, H.J. and Geng, L. (2014) Tropical forcing of the recent rapid Arctic warming in North-Eastern Canada and Greenland. *Nature*, 509(7499), 209–212.

Ding, Q. and Wang, B. (2007) Intraseasonal teleconnection between the summer Eurasian wave train and the Indian monsoon. *Journal of Climate*, 20, 3751–3767.

Dong, B., Sutton, R.T. and Shaffrey, L. (2017) Understanding the rapid summer warming and changes in temperature extremes since the mid-1990s over Western Europe. *Climate Dynamics*, 48(5–6), 1–18.

Dunn-Sigouin, E. and Son, S.W. (2013) Northern hemisphere blocking frequency and duration in the CMIP5 models. *Journal of Geophysical Research—Atmospheres*, 118, 1179–1188.

Enomoto, T. (2004) Interannual variability of the Bonin high associated with the propagation of Rossby waves along the Asian jet. *Journal of the Meteorological Society of Japan*, 82(4), 1019–1034.

Frich, P., Alexander, L., Della-Marta, P., Gleason, B., Haylock, M., Klein Tank, A.M.G. and Peterson, T.C. (2002) Observed coherent changes in climatic extremes during the second half of the twentieth century. *Climate Research*, 19(3), 193–212. https://doi.org/10.3354/cr019193.

Guo, P., Dirmeyer, P.A. and DelSole, T. (2011) Land surface impacts on subseasonal and seasonal predictability. *Geophysical Research Letters*, 38, L24812. https://doi.org/10.1029/2011GL049945.

Gutzler, D.S. and Wallace, J. M. (1981) Teleconnections in the geopotential height field during the Northern Hemisphere winter. *Mon Weather Rev*, 109(2), 784–812.

Han, T., He, S., Wang, H. and Hao, X. (2018) Enhanced influence of early-spring tropical indian ocean SST on the following early-summer precipitation over Northeast China. *Climate Dynamics*, 51, 4065–4076.

Hoskins, B.J. and Ambrizzi, T. (1993) Rossby wave propagation on a realistic longitudinally varying flow. *Journal of the Atmospheric Sciences*, 50, 1661–1671.

Hoskins, B.J. and Karoly, D.J. (1981) The steady linear response of a spherical atmosphere to thermal and orographic forcing. *Journal of the Atmospheric Sciences*, 38(6), 1179–1196.

Hoskins, B.J. and Woollings, T. (2015) Persistent extratropical regimes and climate extremes. *Current Climate Change Reports*, 1(3), 115–124.

Hu, Q. and Feng, S. (2008) Variation of North American summer monsoon regimes and the Atlantic multi-decadal oscillation. *Journal of Climate*, 21, 2373–2383.

Huang, J., Ji, M., Xie, Y., Wang, S., He, Y. and Ran, J. (2015) Global semi-arid climate change over last 60 years. *Climate Dynamics*, 46(3–4), 1131–1150.

Ju, J., Lü, J., Cao, J. and Ren, J. (2005) Possible impacts of the Arctic oscillation on the interdecadal variation of summer monsoon rainfall in East Asia. *Advances in Atmospheric Sciences*, 22(1), 39–48.

Kamae, Y., Shiogama, H., Watanabe, M. and Kimoto, M. (2014) Attributing the increase in Northern hemisphere hot summers since the late 20th century. *Geophysical Research Letters*, 41(14), 5192–5199.

Kosaka, Y. and Xie, S. (2013) Recent global-warming hiatus tied to equatorial Pacific surface cooling. *Nature*, 501, 403–407.

Lau, K.M. and Weng, H.Y. (2002) Recurrent teleconnection patterns linking summertime precipitation variability over East Asia and North America. *Journal of the Meteorological Society of Japan*, 80, 1309–1324.

Lee, S., Gong, T., Johnson, N., Feldstein, S.B. and Pollard, D. (2011) On the possible link between tropical convection and the Northern hemisphere Arctic surface air temperature change between 1958 and 2001. *Journal of Climate*, 24(16), 4350–4367.

Liang, X.S. (2016) Canonical transfer and multiscale energetics for primitive and Quasigeostrophic atmospheres. *Journal of the Atmospheric Sciences*, 73(11), 4439–4468.

Liang, X.S. and Anderson, D.G.M. (2007) Multiscale window transform. *Multiscale Modeling and Simulation*, 6(2), 437–467.

Liang, X.S. and Robinson, A.R. (2005) Localized multiscale energy and vorticity analysis: I. fundamentals. *Dynamics of Atmospheres and Oceans*, 38, 195–230.

Luo, D., Gong, T. and Diao, Y. (2007) Dynamics of eddy-driven low-frequency dipole modes. Part iii: meridional displacement of westerly jet anomalies during two phases of NAO. *Journal of the Atmospheric Sciences*, 64(9), 3232–3248.

Manola, I., Selten, F., Vries, H.D. and Hazeleger, W. (2013) "Waveguidability" of idealized jets. *Journal of Geophysical Research, [Atmospheres]*, 118(18), 10432–10440.

Masato, G., Hoskins, B. and Woollings, T. (2013) Winter and summer Northern hemisphere blocking in CMIP5 models. *Journal of Climate*, 26, 7044–7059.

Petoukhov, V., Petri, S., Rahmstorf, S., Coumou, D., Kornhuber, K. and Schellnhuber, H.J. (2016) Role of quasiresonant planetary wave dynamics in recent boreal spring-to-autumn extreme events. *PNAS*, 113(25), 6862–6867.

Petoukhov, V., Rahmstorf, S., Petri, S. and Schellnhuber, H.J. (2013) Quasiresonant amplification of planetary waves and recent Northern hemisphere weather extremes. *PNAS*, 110(14), 5336–5377.

Qian, C. and Zhou, T. (2013) Multidecadal variability of North China aridity and its relationship to PDO during 1900-2010. *Journal of Climate*, 27(3), 1210–1222.

Sato, K., Inoue, J. and Watanabe, M. (2014) Influence of the Gulf stream on the Barents Sea ice retreat and Eurasian coldness during early winter. *Environmental Research Letters*, 9(8), 084009.

Sato, N. and Takahashi, M. (2006) Dynamical processes related to the appearance of quasi-stationary waves on the subtropical jet in the midsummer Northern hemisphere. *Journal of Climate*, 19(8), 1531–1544.

Scaife, A.A., Woollings, T., Knight, J., Martin, G. and Hinton, T. (2010) Atmospheric blocking and mean biases in climate models. *Journal of Climate*, 23, 6143–6152. https://doi.org/10.1175/2010JCLI3728.1.

Schneider, T., Bischoff, T. and Płotka, H. (2015) Physics of changes in synoptic midlatitude temperature variability. *Journal of Climate*, 28, 2312–2331.

Schubert, S., Wang, H., Koster, R., Suarez, M. and Groisman, P. (2014) Northern Eurasian heat waves and droughts. *Journal of Climate*, 27(9), 3169–3207.

Schubert, S., Wang, H. and Suarez, M. (2010) Warm season subseasonal variability and climate extremes in the northern hemisphere: the role of quasi-stationary waves. *Journal of Climate*, 24(18), 4773–4792.

Shen, B.Z., Lin, Z.D., Lu, R.Y. and Lian, Y. (2011) Circulation anomalies associated with interannual variation of early- and late-summer precipitation in Northeast China. *Science China Earth Sciences*, 54(7), 1095–1104.

Sun, X.Q., Li, S.L., Hong, X.W. and Lu, R.Y. (2019) Simulated influence of the Atlantic multidecadal oscillation on summer Eurasian nonuniform warming since the mid-1990s. *Advances in Atmospheric Sciences*, 36(8), 811–822.

Sutton, R.T. and Hodson, D.L.R. (2005) Atlantic Ocean forcing of North American and European summer climate. *Science*, 309, 115–118.

Takaya, K. and Nakamura, H. (2001) A formulation of a phase-independent wave-activity flux for stationary and migratory Quasigeostrophic eddies on a zonally varying basic flow. *Journal of the Atmospheric Sciences*, 58(6), 608–627.

Trenberth, K.E., Fasullo, J.T., Branstator, G. and Phillips, A. (2014) Seasonal aspects of the recent pause in surface warming. *Nature Climate Change*, 4, 911–916.

Ueda, H., Kamae, Y., Hayasaki, M., Kitoh, A., Watanabe, S., Miki, Y. and Kumai, A. (2015) Combined effects of recent Pacific cooling and Indian Ocean warming on the Asian monsoon. *Nature Communications*, 6, 8854.

Wang, H. and He, S. (2015) The Northern China/Northeastern Asia severe summer drought in 2014. *Journal of Climate*, 28(17), 150522112645005.

Wang, N. and Zhang, Y. (2014) Evolution of Eurasian teleconnection pattern and its relationship to climate anomalies in China. *Climate Dynamics*, 44(3–4), 1017–1028.

Wang, S., Huang, J., He, Y. and Guan, Y. (2014) Combined effects of the Pacific decadal oscillation and El Niño-southern oscillation on global land dry-wet changes. *Scientific Reports*, 4, 6651.

Wang, W. and Kumar, A. (1998) A GCM assessment of atmospheric seasonal predictability associated with soil moisture anomalies over North America. *Journal of Geophysical Research*, 103 (D22), 28,637–28,646.

Watanabe, M. and Kimoto, M. (2000) Atmosphere-ocean thermal coupling in the North Atlantic: A positive feedback. *Quarterly Journal of the Royal Meteorological Society*, 126(570), 3343–3369.

Woollings, T. and Blackburn, M. (2012) The North Atlantic Jet stream under climate change and its relation to the NAO and EA patterns. *Journal of Climate*, 25, 886–902.

Wu, Z. and Huang, N.E. (2009) Ensemble empirical mode decomposition: a noise-assisted data analysis method. *Advances in Adaptive Data Analysis*, 1, 1–41.

Wu, Z., Li, J., Jiang, Z. and Ma, T. (2012) Modulation of the Tibetan plateau snow cover on the ENSO teleconnections: from the east Asian summer monsoon perspective. *Journal of Climate*, 25, 2481–2489.

Xin, X.G., Zhou, T. and Yu, R. (2010) Increased Tibetan plateau snow depth: an indicator of the connection between enhanced winter NAO and late-spring tropospheric cooling over East Asia. *Advances in Atmospheric Sciences*, 27, 788–794.

Zhang, J., Chen, H. and Zhang, Q. (2019a) Extreme drought in the recent two decades in northern China resulting from Eurasian warming. *Climate Dynamics*, 52, 2885–2902.

Zhang, J., Chen, H. and Zhao, S. (2019b) A tripole pattern of summertime rainfall and the teleconnections linking northern China to the Indian subcontinent. *Journal of Climate*, 32, 3637–3653. https://doi.org/10.1175/JCLI-D-18-0659.1.

Zhang, J., Chen, Z., Chen, H., Ma, Q. and Teshome, A. (2020) North Atlantic multidecadal variability enhancing decadal extratropical extremes in boreal late summer in the early twenty-first century. *Journal of Climate*, 33, 6047–6064.

Zhang, J., Li, L., Wu, Z. and Li, X. (2015) Prolonged dry spells in recent decades over north-Central China and their association with a northward shift in planetary waves. *International Journal of Climatology*, 35, 4829–4842.

Zhang, J., Liu, C. and Chen, H. (2018a) The modulation of Tibetan plateau heating on the multi-scale northernmost margin activity of East Asia summer monsoon in northern China. *Global and Planetary Change*, 161, 149–161.

Zhang, J., Yang, Z. and Wu, L. (2018b) Skillful prediction of hot temperature extremes over the source region of ancient silk road. *Scientific Reports*, 8(1), 6677.

Zhao, P., Yang, S. and Yu, R. (2010) Long-term changes in rainfall over eastern China and large-scale atmospheric circulation associated with recent global warming. *Journal of Climate*, 23(6), 1544–1562.

Zhuo, H., Liu, Y. and Jin, J. (2016) Improvement of surface skin temperature simulation over the Tibetan plateau and the associated impact on circulation in East Asia. *Atmospheric Science Letters*, 17(2), 162–168.

How to cite this article: Zhang J, Zhao S, Chen Z. Increasing energy transfer over Eurasia and the North Atlantic enhancing the Eurasian low-frequency wave and boreal summer droughts in China. *Int J Climatol*. 2020;1–18. https://doi.org/10.1002/joc.6905